

Monitoring the SNS basement neutron background with the MARS detector

D. Akimov,^a P. An,^{b,c} C. Awe,^{b,c} P.S. Barbeau,^{b,c} B. Becker,^d V. Belov,^{e,a} I. Bernardi,^d M.A. Blackston,^f C. Bock,^g A. Bolozdynya,^a J. Browning,^h B. Cabrera-Palmer,ⁱ D. Chernyak,^{g,1} E. Conley,^b J. Daughhetee,^f J. Detwiler,^j K. Ding,^g M.R. Durand,^j Y. Efremenko,^{d,f} S.R. Elliott,^k L. Fabris,^f M. Febbraro,^f A. Gallo Rosso,^l A. Galindo-Uribarri,^{f,d} M.P. Green,^{c,f,h} M.R. Heath,^f S. Hedges,^{b,c} D. Hoang,^m M. Hughes,ⁿ B.A. Johnson,ⁿ T. Johnson,^{b,c} A. Khromov,^a A. Konovalov,^{a,e} E. Kozlova,^{a,e} A. Kumpan,^a L. Li,^{b,c} J.M. Link,^o J. Liu,^g K. Mann,^h D.M. Markoff,^{p,c} J. Mastroberti,ⁿ P.E. Mueller,^f J. Newby,^f D.S. Parno,^m S.I. Penttila,^f D. Pershey,^b R. Rapp,^m H. Ray,^q J. Raybern,^b O. Razuvaeva,^{a,e} D. Reyna,ⁱ G.C. Rich,^c J. Ross,^{p,c} D. Rudik,^a J. Runge,^{b,c} D.J. Salvat,ⁿ A.M. Salyapongse,^m J. Sander,^g K. Scholberg,^b A. Shakirov,^a G. Simakov,^{a,e} G. Sinev,^{b,2} W.M. Snow,ⁿ V. Sosnovstsev,^a B. Suh,ⁿ R. Tayloe,ⁿ K. Tellez-Giron-Flores,^o I. Tolstukhin,^{n,3} E. Ujah,^{p,c} J. Vanderwerp,ⁿ R.L. Varner,^f C.J. Virtue,^l G. Visser,ⁿ T. Wongjirad,^r Y.-R. Yen,^m J. Yoo,^s C.-H. Yu,^f J. Zettlemoyer^{n,4}

^aNational Research Nuclear University MEPhI (Moscow Engineering Physics Institute), Moscow, 115409, Russian Federation

^bDepartment of Physics, Duke University, Durham, NC, 27708, USA

^cTriangle Universities Nuclear Laboratory, Durham, NC, 27708, USA

^dDepartment of Physics and Astronomy, University of Tennessee, Knoxville, TN, 37996, USA

^eInstitute for Theoretical and Experimental Physics named by A.I. Alikhanov of National Research Centre "Kurchatov Institute", Moscow, 117218, Russian Federation

^fOak Ridge National Laboratory, Oak Ridge, TN, 37831, USA

^gPhysics Department, University of South Dakota, Vermillion, SD, 57069, USA

^hDepartment of Physics, North Carolina State University, Raleigh, NC, 27695, USA

ⁱSandia National Laboratories, Livermore, CA, 94550, USA

^jCenter for Experimental Nuclear Physics and Astrophysics & Department of Physics, University of Washington, Seattle, WA, 98195, USA

^kLos Alamos National Laboratory, Los Alamos, NM, 87545, USA

^lDepartment of Physics, Laurentian University, Sudbury, Ontario, P3E 2C6, Canada

^mDepartment of Physics, Carnegie Mellon University, Pittsburgh, PA, 15213, USA

ⁿDepartment of Physics, Indiana University, Bloomington, IN, 47405, USA

^oCenter for Neutrino Physics, Virginia Tech, Blacksburg, VA, 24061, USA

^pDepartment of Mathematics and Physics, North Carolina Central University, Durham, NC, 27707, USA

^qDepartment of Physics, University of Florida, Gainesville, FL, 32611, USA

^rDepartment of Physics and Astronomy, Tufts University, Medford, MA, 02155, USA

^sDepartment of Physics and Astronomy, Seoul National University, Seoul, 08826, Korea

E-mail: bcabrer@sandia.gov

¹Now at: Moscow, "Theoretical and Experimental Physics, 117218, Russia", Department of Physics and Astronomy, Tuscaloosa and Institute for Nuclear Research of NASU, Kyiv, 03028, Ukraine

²Now at: South Dakota School of Mines and Technology, Rapid City, SD, 57701, USA

³Now at: Argonne National Laboratory, Argonne, IL, 60439, USA

⁴Now at: Fermi National Accelerator Laboratory, Batavia, IL, 60510, USA

ABSTRACT: We present the analysis and results of the first dataset collected with the MARS neutron detector deployed at the Oak Ridge National Laboratory Spallation Neutron Source (SNS) for the purpose of monitoring and characterizing the beam-related neutron (BRN) background for the COHERENT collaboration. MARS was positioned next to the COH-CsI coherent elastic neutrino-nucleus scattering detector in the SNS basement corridor. This is the basement location of closest proximity to the SNS target and thus, of highest neutrino flux, but it is also well shielded from the BRN flux by infill concrete and gravel. These data show the detector registered roughly one BRN per day. Using MARS' measured detection efficiency, the incoming BRN flux is estimated to be 1.20 ± 0.56 neutrons/m²/MWh for neutron energies above ~ 3.5 MeV and up to a few tens of MeV. We compare our results with previous BRN measurements in the SNS basement corridor reported by other neutron detectors.

KEYWORDS: Neutron detector, neutron spectrometer, gadolinium, plastic scintillator, capture gated, coherent elastic neutrino-nucleus scattering, CEvNS

Contents

1	Introduction	1
2	MARS detector for BRN background studies at SNS	2
2.1	Neutron-detection concept	2
2.2	Hardware description	3
2.3	Electronic read-out and trigger scheme	3
3	Experimental data	5
3.1	MARS location in the SNS basement corridor	5
3.2	Data-collection period and data quality	6
4	Data Processing	7
4.1	Capture energy cut selection from the muon-induced neutron events	9
5	Measured BRN rate	13
6	BRN flux at the Neutrino Alley	17
6.1	Flux estimation from MARS data	17
6.2	Flux estimation from other detectors	19
7	Conclusions	19

1 Introduction

Understanding the fast and higher-energy ($\gtrsim 10$ MeV) neutron background is of particular importance for experiments aiming to measure coherent elastic neutrino-nucleus scattering (CEvNS) since neutron elastic scattering produces nuclear recoils similar to the CEvNS signature. For the COHERENT experiment [1–8] at the Oak Ridge National Laboratory Spallation Neutron Source (SNS), the most impactful neutrons are those produced in the SNS target at the same time as the neutrinos, the latter originating also at the target from the decay of pions.

The 1-GeV, 1.4-MW proton beam of the SNS accelerator strikes a liquid-Hg target in 360 ns FWHM pulses at 60 Hz to produce neutrons that are moderated and delivered to neutron experiments. As part of each proton-on-target (POT) event, prompt muon neutrinos (ν_μ) and delayed muon antineutrinos and electron neutrinos ($\bar{\nu}_\mu$ and ν_e) are also produced from the decay of pions [3, 7], benefiting neutrino-physics experiments like COHERENT. To mitigate the impact of the beam-related neutron (BRN) background, the COHERENT detectors are deployed in the SNS basement corridor dubbed “Neutrino Alley”. This location is shielded from the SNS target by the combination of the target monolith and infill concrete and gravel, while it also provides the benefit of 8 meter of water equivalent overburden against cosmic rays [9]. Nevertheless, knowledge of

the rate and spectral distribution of the beam neutrons reaching the various COHERENT detectors is important for detector design, modeling and data analysis. For the CEvNS measurement with the COH-CsI detector [1] deployed at the location with the lowest BRN flux according to previous measurements [9], the BRN background was about 6% of the predicted CEvNS rate, with a 25% systematic uncertainty. However, for the CEvNS observation with argon [4], the BRN rate was about four times larger than the predicted CEvNS rate. Developing a firm understanding of the neutron flux in Neutrino Alley is thus critical for future high-precision cross-section measurements.

In this paper, we provide the analysis and results of neutron data collected with the Multiplicity and Recoil Spectrometer, or MARS, deployed at the SNS for the purpose of monitoring and characterizing the BRN background for the COHERENT collaboration. As will be described in section 2, the MARS configuration deployed at the SNS and discussed throughout this paper includes one module of plastic scintillator layers with interleaved gadolinium (Gd) coated Mylar sheets, and operates in the “capture-gated” mode explained in section 2.1. This differs from the original configuration of this detector created for a different experiment [10], which also included a plane of lead bricks sandwiched between two modules of plastic scintillator layers and exploited the “multiplication” of neutrons in the lead bricks due to incoming high-energy neutrons.

Details of the MARS experimental deployment at the SNS are covered in section 3. Sections 4 and 5 are devoted to the processing and analysis of the first beam-on MARS dataset collected during the year 2018. The measured BRN rates at the MARS deployment location beside the COH-CsI neutrino detector of [1] are reported in section 6. A comprehensive study of the MARS response—including the measurement and modeling of its light-collection efficiency, energy resolution and capture-gated signal response as a function of active volume region, the derivation of the energy calibration as well as the modeling of the detection-efficiency energy and threshold dependence—will be the subject of future work. In this work, for the purpose of providing an estimate of the incident BRN flux, section 6 contains a summary of MARS’ detection efficiency measurement done with 14 MeV neutrons. MARS data taken subsequently at different Neutrino Alley locations with different BRN flux levels will be treated in future work.

2 MARS detector for BRN background studies at SNS

2.1 Neutron-detection concept

For MARS’ neutron-detection mechanism, we use the so-called capture-gated mode. When a fast neutron elastically interacts with hydrogen nuclei in MARS’ large plastic scintillator volume, the recoiling protons generate a prompt scintillation pulse. If the neutron does not escape, it will bounce around the detector while quickly thermalizing. In the presence of a material with a large thermal-neutron capture cross section like Gd, there is a high probability that de-excitation gamma rays will be produced. For Gd, the maximum total energy of the emitted gamma rays is ~ 8 MeV. The neutron-capture process in MARS has a time constant τ_{nCapt} that depends on the Gd concentration, and it was reported to be $18.7 \mu\text{s}$ for the MARS configuration used in [10]. Thus, by employing the timing and energy of the Gd gamma-ray scintillation pulses, the population of fully thermalized and absorbed neutrons can be isolated. When the neutron’s kinetic energy is fully and quickly transferred to the scintillator in elastic scatterings, the integral of the prompt pulse is a direct

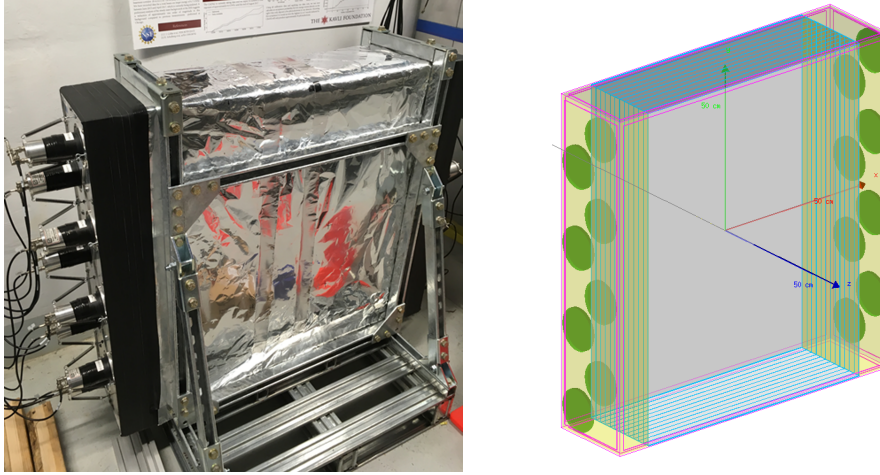


Figure 1. Left: A photograph of the MARS detector in Neutrino Alley. The bases of the PMTs are visible on the left-hand side of the photograph, and a unistrut support structure holds the stacked scintillators. Right: Geant4 [11] model of the detector. The cyan boxes represent the plastic scintillator layers. The side acrylic light guides are in yellow, with green circles representing the PMT windows.

measure of the incoming neutron energy. Since the fraction of neutrons thermalizing purely via elastic interactions decreases with neutron energy, being of the order of a few percent for ~ 50 MeV neutrons, the capture-gated mode as considered in this work is limited to provide rate and spectral information on BRN energies no larger than a few tens of MeV.

2.2 Hardware description

The MARS detector, pictured in Fig. 1 (left), consists of twelve 2-cm-thick BC-408 plastic scintillator layers interleaved with Gd-coated Mylar sheets. The overall dimensions of the detection volume are $L \times W \times H = 75 \times 25 \times 100 \text{ cm}^3$. This module stands vertically on its $L \times W$ side held by a Unistrut frame, with each $W \times H$ face covered by a $10 \times 25 \times 100 \text{ cm}^3$ acrylic light guide that optically couples the scintillator layers. On each side, eight 5-inch diameter ADIT B133D01 photomultiplier tubes (PMTs) are coupled to the light guides by silicon grease. Black tape covers the scintillator and acrylic volumes for light-tightness, which are further wrapped with an aluminum sheet for fire safety.

2.3 Electronic read-out and trigger scheme

Data readout, diagrammatically shown in Fig. 2, is done with two 14-bit, 250 MHz Struck SIS3316 sixteen-channel waveform digitizers [12] mounted in a VME crate. All channels of the first digitizer are used to digitize the sixteen PMT signals. The second digitizer asynchronously records two SNS-provided signals, arbitrarily named “event-39” and “event-61” triggers, which are synchronized with the SNS beam. The event-39 triggers are provided uninterrupted at 60 Hz during beam-on and beam-off periods. The event-61 triggers are supplied during beam-on operation whenever there is a POT event, which occurs also with a 60 Hz frequency but with one event skipped in every (1/600) second period.

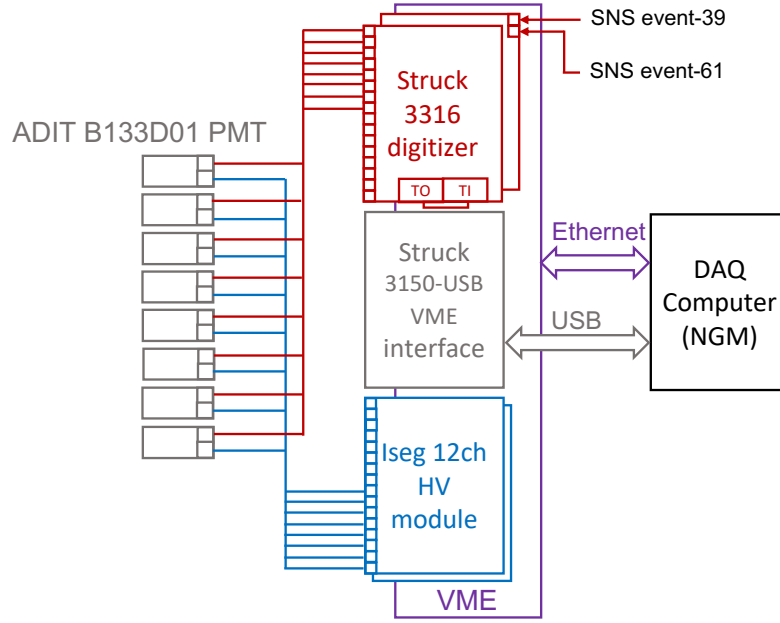


Figure 2. Diagram of MARS’s electronic read-out and high-voltage (HV) setup. Only eight of the 16 PMT channels are represented for simplicity. The data acquisition (DAQ) is managed by the NGM software package [13]. TO and TI represent the Trigger Out and Trigger In connectors, respectively.

The signals from a pair of neighboring PMTs on one side of the scintillator module and the corresponding pair at the same height on the opposite side are joined into the same digitizer’s channel group, for a total of four groups. Using the digitizer’s trigger logic, a trapezoidal Finite Input Response (FIR) filter is applied on each four-channel sum signal to generate a trigger signal [12]. The FIR filter’s peaking and gap times were each set to 4 samples, or 16 ns. With the CFD (Constant Fraction Discriminator) feature enabled, the trapezoidal threshold value is set to achieve the lowest physical signal threshold that still produces negligible dead time — the physical signal threshold in energy units will be discussed in section 4. The internally generated trigger is routed to the external trigger input to start the sampling of all sixteen channels. The pre-trigger delay was adjusted to contain most of the scintillation pulse within the 150-sample active trigger gate window, including 50 baseline pre-samples.

For each recorded event, the raw channel data contain: channel ID, timestamp, peak sample index, peak height value, and six accumulator sums. Each accumulator stores the integral of 25 samples, with accumulator 0 integrating samples 0-24, accumulator 1 integrating samples 25-49, and so on. At the first stage of processing, each PMT channel integral is calculated as the sum of accumulators 2 to 5 (equivalent to integrating 100 samples) minus the baseline integral. The latter is computed as the sample average of the combined first two accumulators multiplied by 100. The sum of the sixteen baseline-subtracted integrals is taken to represent the total energy of the scintillator pulse in the digitizer output units which we denote here as “adc” units. The time intervals since the previous event-39 signal, the previous event-61 signal and the previous scintillator pulse are also recorded. A further description of the pre-processed data is given at the start of section 4.

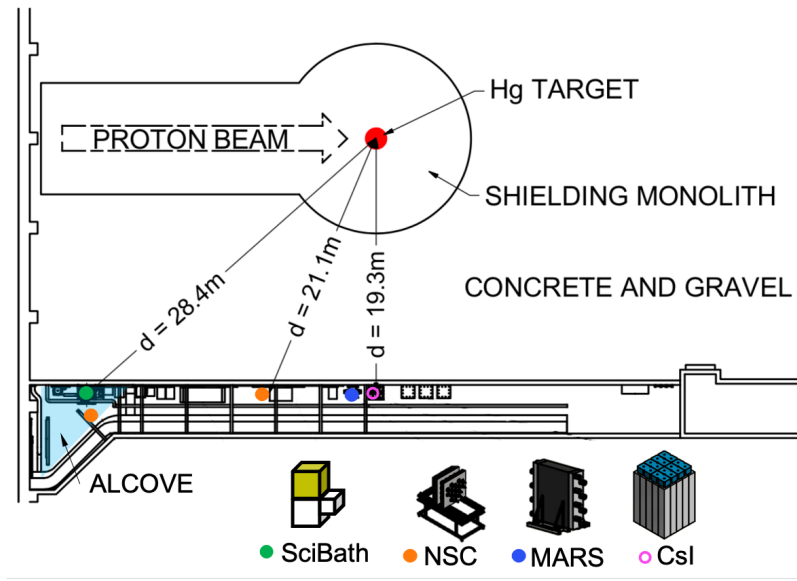


Figure 3. Diagram of a top-down view of the SNS Neutrino Alley showing MARS and CsI detector locations during 2018. Also shown are the earlier deployment locations of the neutron scatter camera (NSC) [14] and of the SciBath detector [15], employed as part of COHERENT’s first neutron-background measurements at the SNS. The blue shade indicates the Neutrino Alley alcove area. Some of COHERENT’s other detectors are omitted here for simplicity.

3 Experimental data

3.1 MARS location in the SNS basement corridor

In the fall of 2017, MARS was deployed in the SNS basement corridor next to the COH-CsI detector system (Fig. 3, right), at 19.5 m from the SNS target, with concrete and gravel filling most of the space between the Neutrino Alley and the SNS target monolith, plus 8 meter-water-equivalent overburden. A previous neutron-background measurement campaign [9] that included three different locations along the SNS basement corridor showed the vicinity of the COH-CsI system as having the lowest SNS BRN background. In this regard, the BRN rates measured by MARS here are expected to be highly suppressed.

A high flux of 511 keV gamma rays is present all along the Neutrino Alley. This gamma field is emitted from a 6-inch diameter pipe that runs through the corridor near the concrete ceiling and carries radioactive gas from the SNS-target water moderating system. These 511 keV gamma rays mainly originate from β^+ decay positrons (*e.g.*, from ^{11}C) and create a high and continually present “Hot Off Gas” (HOG) background during beam-on periods. Given that the MARS design does not include shielding material of any kind, its response has been found to be highly sensitive to variations in the HOG background during the analyzed period, as will be presented in section 4. Adding 1 cm of high-Z shielding material like lead around the MARS active volume would significantly attenuate the 511 keV gamma flux, but it would also create a source of multiple low energy neutrons ($\sim 1\text{-}2$ MeV, [10, 16]) from the spallation reactions of the high-energy BRNs. Without a careful quantization of this effect, MARS was left without shielding, and instead, efforts have focused on

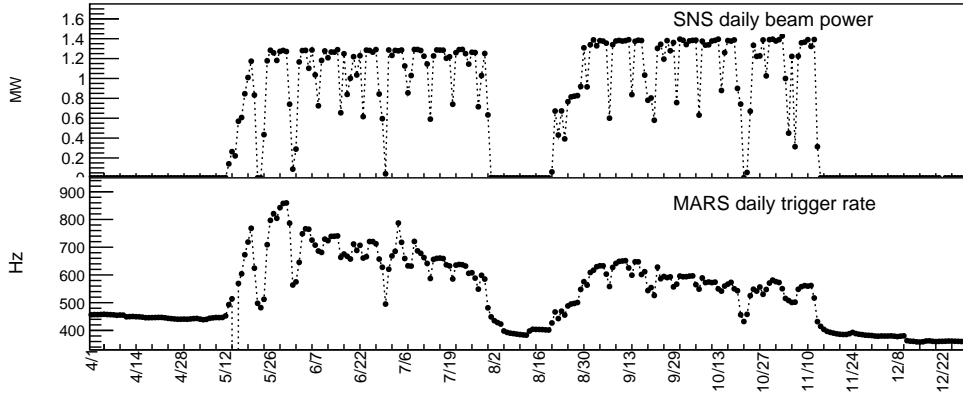


Figure 4. Top: SNS daily delivered beam power. Bottom: daily PMT-sum trigger rate as reported by the COHERENT Grafana [17] dashboard. The horizontal axis represents the calendar dates from April 1, 2018 to December 31, 2018, and are labeled as month/day. The PMT-rate gradual decrease indicates a gain shift in the MARS response.

surrounding the HOG pipe with a lead layer to suppress the 511 keV background.

3.2 Data-collection period and data quality

MARS production data collection started at the end of December 2017 during an SNS shutdown period, so that sufficient beam-off data were collected before the SNS beam turned on in May 2018. The analysis presented here uses data from April 01, 2018 to December 31, 2018. The top panel of Fig. 4 shows the beam power for each day of the period under analysis. The SNS operational beam power level intended for the beam-on period covering June and July was 1.3 megawatt (MW), increasing to 1.4 MW for the subsequent beam-on period from September to early November.

The PMT trigger rates, presented for each day in the second panel of Fig. 4, show a significant jump during the two 2018 beam-on periods compared to the beam-off data, due to the intense HOG gamma-background flux. The 2018 PMT rates also showed a gradual decrease during beam-on periods when the beam power was stable — and thus, with the HOG background intensity also expected to be stable — indicating a gain shift in the MARS response. We show in section 4.1 how these 511 keV background signals not only increase the total event rate but also pile-up on most of the PMT signal pulses, causing a positive shift in the pulse-integral energy spectrum. Thus, in order to elude the HOG-background shifting effect on the spectrum, we compared the April, August and December beam-off data and noted that the event rate always decreased relative to the previous beam-off period. Since the digitizer threshold settings were kept unchanged during the whole data-collection period, we hypothesize that the event-rate decrease arose from an effective decrease in overall gain over time, though its origin was not investigated.

During year 2018 production operation, a new run was started every 24 hours. The second panel of Fig. 4 shows the data’s daily trigger rate, illustrating that there were not any major data-collection interruptions. In our analysis, the data were aggregated in 14-day intervals. Most of the intervals correspond to sets of continuous 14 days; in the cases when there was a calendar-day gap, the next calendar day at the end of the interval was aggregated in order to keep the total aggregated time to be approximately 14 days.

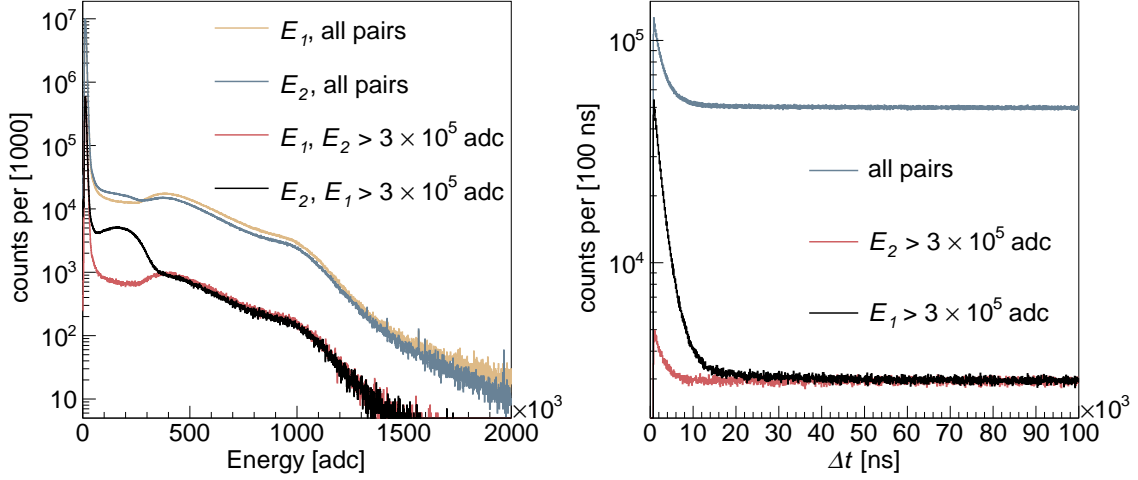


Figure 5. Left: Histograms of the first pulse’s energy E_1 and the second pulse’s energy E_2 of the scintillator pulse pairs from the April 2018 beam-off data. The first two histograms in the legend include all pairs. The last (black) E_2 histogram only includes pairs with $E_1 > 3 \times 10^5$ adc that select muon-track high-energy depositions. The (red) E_1 histogram, with the same cut applied instead to E_2 , illustrates the differences in the E_1 and E_2 populations. Right: Histograms of the inter-pulse time Δt for the same cuts. The black histograms of both panels clearly show the spectral (E_2) and time (Δt) profiles expected for Michel electrons.

4 Data Processing

In data pre-processing, any two scintillator pulses separated by no more than $200 \mu s$ are grouped into a “pulse pair” — for example, a sequence of 3 scintillation pulses where the first and last were closer than $200 \mu s$ would yield 3 pulse pairs. Each pair is described by the variables $(t_1, E_1, \Delta t, E_2)$, where t_1 is the time interval between the first pulse of the pair, or prompt pulse, and the preceding event-39 trigger (and thus, $t_1 < 1/60$ s), E_1 represents the first pulse’s energy in “adc” units, Δt is the inter-pulse time (restricted to be $\Delta t < 200 \mu s$) and E_2 is the energy of the second pulse, or delayed pulse, also in “adc” units. When a capture-gated neutron detection occurs, (t_1, E_1) represent the prompt neutron-pulse time and energy, while $(\Delta t, E_2)$ represent the Gd neutron-capture time and the energy of the Gd-decay gamma-ray pulse. The $200 \mu s$ maximum bound on Δt will miss a negligible number of neutron-capture events since it is more than 10 times the previously measured Gd neutron-capture time constant.

The derivation of the energy calibration to convert from “adc” units to the energy deposit expressed in scintillation light output units “MeV electron equivalent”, or MeVee, is out of the scope of this paper. For the purpose of assessing the consistency of this paper’s results, the scaling $\sim 10^4$ adc per 1 MeVee provides a crude approximation of the energy calibration. This scaling places our trigger threshold at ~ 1 MeVee (10^4 adc), or ~ 3.5 MeV in proton recoil energy [18, 19]. As an illustration, Fig. 5 shows the E_1 , E_2 and Δt histograms of all pairs for one beam-off month. Cosmic muons traversing MARS can generate large pulses and represent the main contribution to the high-energy end of the E_1 and E_2 spectra. Muons decaying within the detector produce highly energetic Michel electrons with a decay time constant $\tau_{\mu^-} = 2.2 \mu s$ [20] and a kinetic-energy cutoff

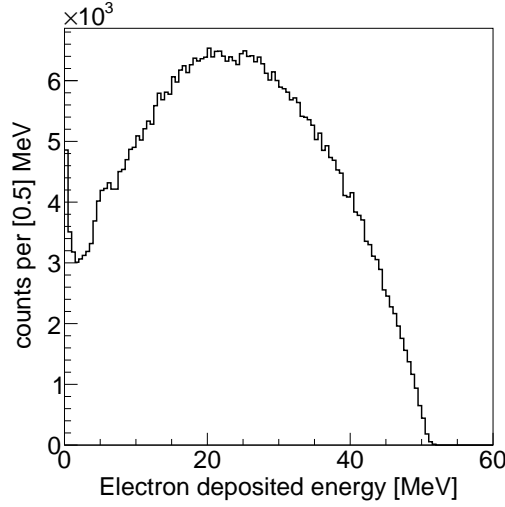


Figure 6. Geant4 simulation of Michel electron tracks that are randomly started within MARS scintillator volume. The simulated electron deposited energy histogram shows the round peak at ~ 20 MeV. Since no energy smearing and light-collection non-uniformity effects have been included, the deposited energy units are expressed in MeV, instead of the MeVee units used for the detected light output.

at ~ 50 MeV [21]. These events are included in our selected data since they also have a double-hit (E_1, E_2) signature corresponding to the muon’s ionization E_1 as the muon penetrates the detection medium and stops, followed by the Michel electron deposition E_2 . The black histogram of the left panel of Fig. 5 shows the prominent and wide Michel electron peak at $E_2 \sim 20 \times 10^4$ adc, obtained by restricting $E_1 > 30 \times 10^4$ adc to select muon-track high-energy depositions. The Δt profile of these pairs, presented in the right panel of Fig. 5, exhibits the Michel electron timing profile. In Fig. 6, the Geant4 [11] simulation of Michel electron tracks started at random locations within the scintillator volume shows their ionization energy spectrum peaking near ~ 20 MeV, consistent with our crude energy scaling.

This prominent Michel electron peak can also be used to evaluate the magnitude of gain variations over the data-collection period. To avoid being affected by the spectral shifts due to the HOG background, the gain changes are evaluated using beam-off data. The left panel of Fig. 7 shows the effective gain decrease of the August 16-22 beam-off data with respect to the May 7-13 beam-off data. To compute the relative gain-correction factor g_c between those two periods, we minimize the χ^2 between the May 7-13 spectrum and the g_c -scaled August 16-22 spectrum, resulting in $g_c = 1.041$. Similarly, the right panel of Fig. 7 shows the effective gain decrease of the December 3-9 beam-off data with respect to the August 16-22 beam-off data, for which $g_c = 1.026$. However, it is not possible to correct for gain changes during beam-on periods due to the HOG-background effect on the spectrum, as will be shown in the next section. Instead, the muon-induced neutron background is used to derive the change in the E_2 cut over time.

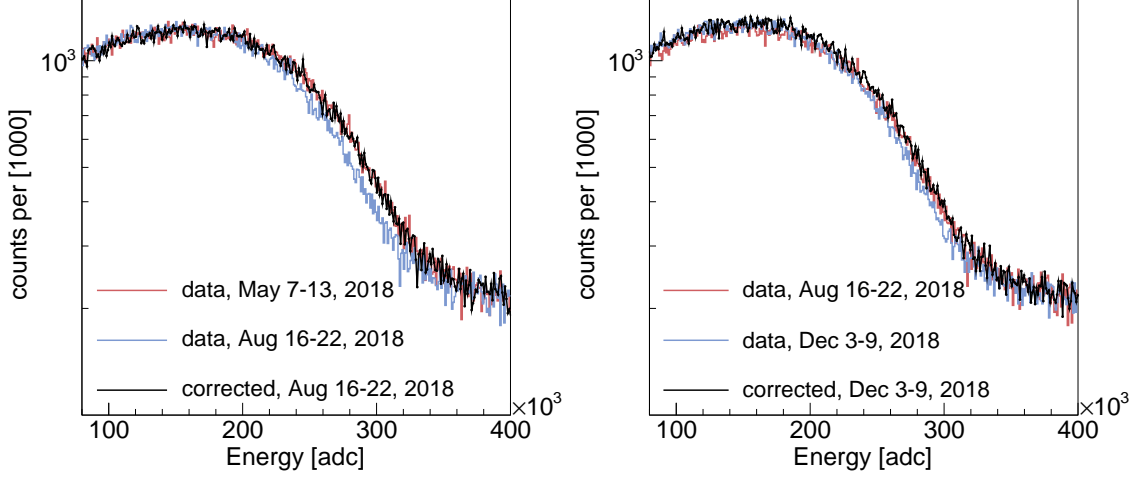


Figure 7. Michel electron spectrum shift from the start (red) to the end (blue) of each beam-on period due to a gradual hardware gain reduction. The gain-corrected spectrum corresponding to the end of each beam-on period is presented in black.

4.1 Capture energy cut selection from the muon-induced neutron events

Cosmic muons also produce spallation neutrons in the detector and in surrounding materials like the concrete walls [22–25]. The detection of this neutron population constitutes a steady-state background that does not depend on the SNS beam status, and thus, can be employed to derive the Δt and E_2 neutron-capture cuts for the detection of the beam neutrons. In this section, we describe a procedure to adjust the E_2 neutron-capture cuts in order to compensate for time-dependent spectral shifts present in our data. Our method derives the time-dependent E_2 cuts that match the measured muon-induced neutron rate to a chosen reference value.

As in the case of Michel electrons, the muon-induced neutron interactions are selected by tagging events with high energy depositions from muon ionization. While the muon-induced neutrons would eject prompt protons before the Gd neutron-capture gamma-ray emission, triple-pulse events that would correspond to a muon track followed by prompt proton recoils and a Gd gamma-ray shower are not observed. On the other hand, we detect a useful rate of pulse pairs with $E_1 > 3 \times 10^5$ adc followed by E_2 pulses with the Δt time structure consistent with neutron capture in Gd. These represent muon-track high-energy depositions, possibly piling up with prompt proton recoils from spallation neutrons either created in the detector or in the surrounding materials, followed by their capture in Gd.

The left panel of Fig. 8 contains the Δt -vs.- E_2 histogram $H_T(E_2, \Delta t)$ of pairs for which the first pulse’s energy is constrained to $E_1 > 3 \times 10^5$ adc in order to select muon-track energy depositions. Since the background rate is higher at low energies, this 2D histogram shows a high-rate band of uncorrelated events near the energy threshold. The right panel of Fig. 8 shows the Δt -projections for two different E_2 ranges: one range is overlapping with the region of E_2 depositions resulting from neutron captures — as will be shown below — and the other range is selected well above the neutron-capture E_2 region. While the Michel electron events are irreducibly present in both ranges,

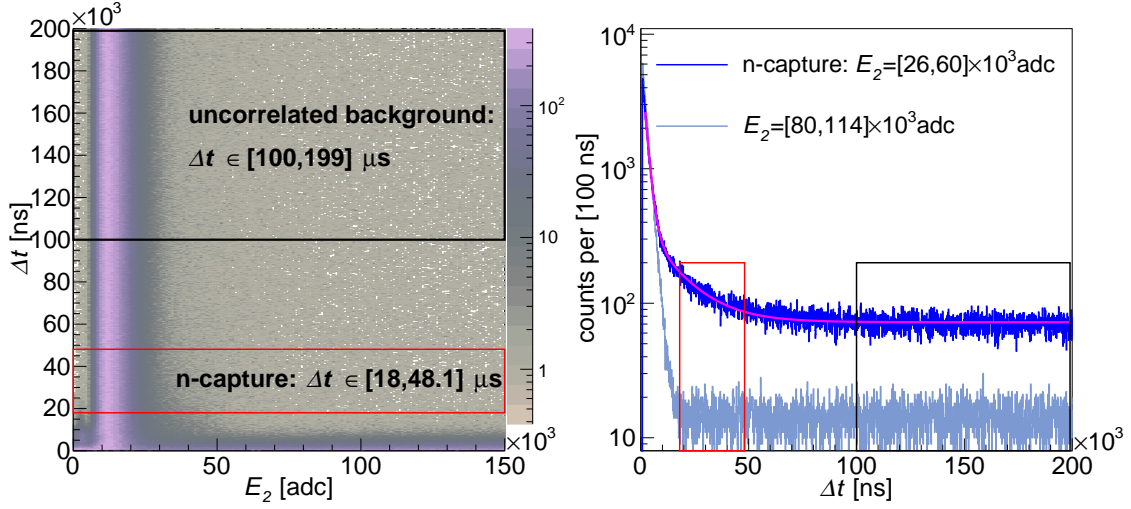


Figure 8. Left: Histogram $H_T(E_2, \Delta t)$ of the inter-pulse time Δt versus the second pulse’s energy E_2 with the first pulse’s energy $E_1 > 3 \times 10^5$ adc selected to represent muon tracks for the April 2018 beam-off data. Right: Δt -projections for two different E_2 ranges. A double exponential fit (pink) of the $E_2 \in [26, 60] \times 10^3$ adc Δt -projection results in $\tau_{\mu^-} = (1.99 \pm 0.01) \mu s$ and $\tau_{Gd} = (15.49 \pm 0.41) \mu s$. The neutron-capture ranges are labeled as n-capture.

time-correlated events with a time constant fit value $\tau_{Gd} = (15.49 \pm 0.41) \mu s$ are present when we set $E_2 \in [26, 60] \times 10^3$ adc, corresponding to muon-induced neutron captures.

The left panel of Fig. 9 shows the E_2 -projections for the two different Δt ranges marked in the 2D histogram of Fig. 8. The neutron-capture Δt range, enclosed in a red bordered rectangle in Fig. 8, is taken to start at $\sim 8 \times \tau_{\mu^-}$ in order to reject Michel electron pairs, and ends at $\sim 3 \times \tau_{Gd}$. The uncorrelated Δt range, enclosed in a black bordered rectangle, represents the flat distribution of accidental, hence uncorrelated, background event pairs. The residual counts between these two E_2 histograms— after properly scaling the background histogram to account for its larger Δt projection range— constitute the muon-induced neutron-capture event count, that, as expected, has the same magnitude for a beam-off month (April 2019) and a beam-on month (July 2019). However, as illustrated in the right panel of Fig. 9, the E_2 values of the beam-on residual counts are shifted up compared to the beam-off E_2 values by $\sim 5 \times 10^3$ adc, which corresponds to about 0.5 MeVee in light-output energy units. This systematic increase in the pulse-integral values is due to a high pile-up rate of HOG-background 511 keV gamma rays.

As a consequence, the muon-induced neutron-capture counts integrated within a fixed E_2 range vary over time depending on the intensity of the HOG background. That behavior is demonstrated by the red plot of Fig. 10, where the two-week muon-induced neutron-capture counts, computed for the fixed cut $E_2 = [26, 60] \times 10^3$ adc, show a similar profile over time as the PMT rates of Fig. 4.

The number of muon-induced neutron events produced in MARS is independent of beam power, though it would depend on changes in the overburden and in the cosmic-ray rate. Data from ground-based detectors that monitor cosmic-ray activity [26] show less than 1% variation in the year 2018 [27]. Thus, since MARS remained under the same overburden during the 2018 data

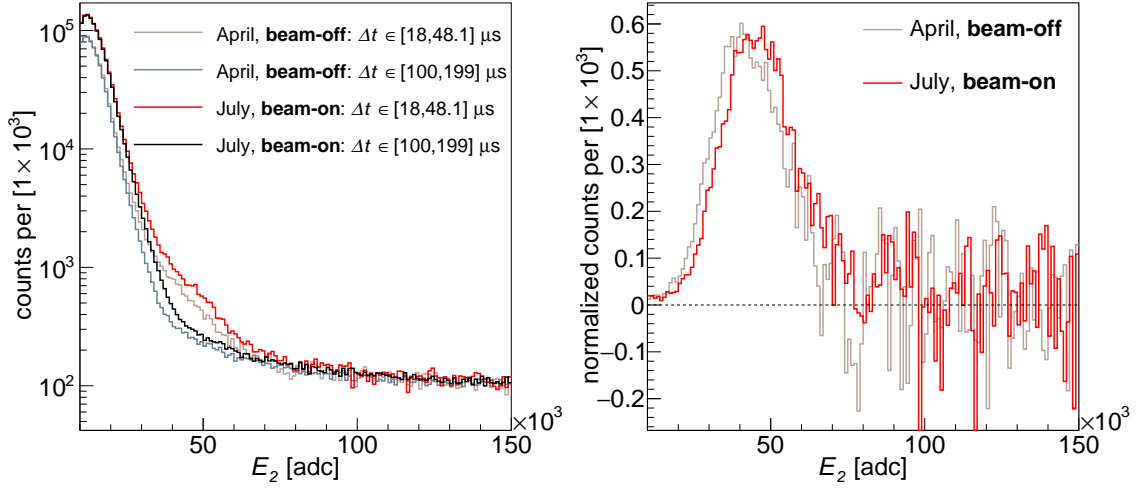


Figure 9. Left: E_2 -projections for the two Δt ranges highlighted in the left panel of Fig. 8, for the April 2018 beam-off and the July 2018 beam-on data. Right: residual counts between the two projections normalized by the neutron-capture projection bin content, for the April 2018 beam-off and the July 2018 beam-on data. Although the E_1 values should also shift as E_2 with the HOG background, using the same $E_1 > 3 \times 10^5$ adc cuts for beam-on and beam-off data yields similar residuals, *i.e.*, similar muon-induced neutron-capture counts.

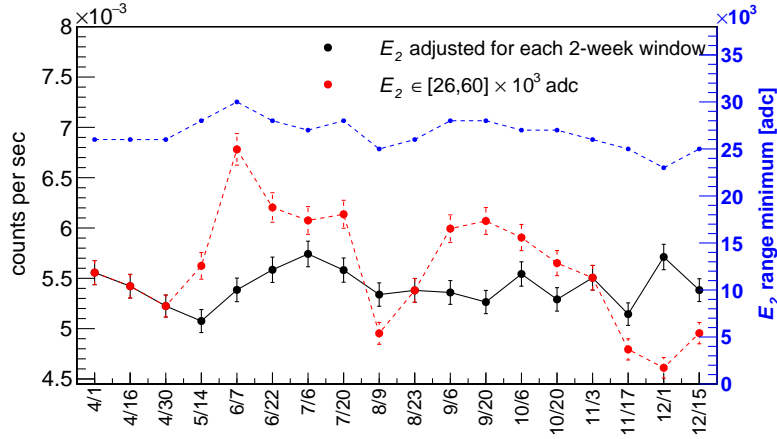


Figure 10. Muon-induced neutron-capture counts integrated over two-week intervals for E_2 cuts adjusted to maintain a “constant” event count, with mean and standard deviation equal to $(5.4 \pm 0.2) \times 10^3$. As a comparison, the counts for a fixed E_2 cut are also plotted. Note that the first three points correspond to two-week intervals overlapping with the April 1-May 6 reference period, and thus, the derived E_2 cuts did not change. The E_2 range minima adjusted for each two-week interval are plotted in blue.

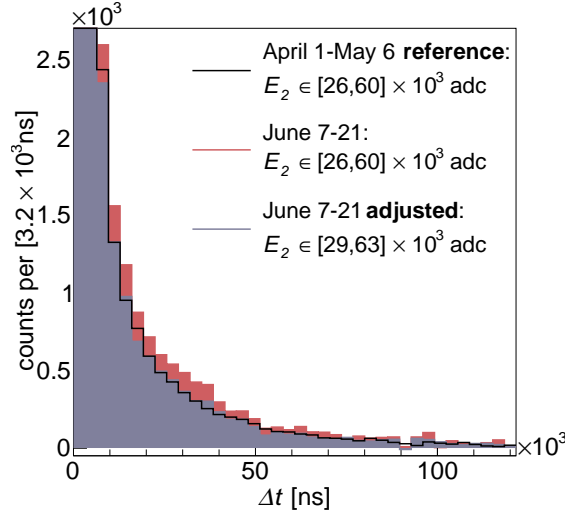


Figure 11. Background-subtracted Δt -projections of pairs with the prompt pulse $E_1 > 3 \times 10^5$ adc selected to represent muon tracks, from April 1-May 6 beam-off and June 7-21 beam-on data. The June 7-21 Δt -projection for the adjusted E_2 cuts matches the April 1-May 6 reference Δt -projection.

run, we can employ muon-induced neutron events to adjust the E_2 neutron-capture cuts for each two-week data interval.

To determine the reference muon-induced neutron rate, we select the average of five beam-off weeks from April 1 to May 6. The reference E_2 and Δt cuts are derived by maximizing the signal-to-noise ratio $S_0 = (T - B)/\sqrt{\sigma_T^2 + \sigma_B^2}$. In this expression, T is the total pair count within the to-be-determined E_2 and Δt neutron-capture reference cuts, denoted as \mathcal{E}_{ref} and \mathcal{T}_{ref} respectively. B is the corresponding uncorrelated background count estimation determined for the same \mathcal{E}_{ref} range but using $\Delta t = [100, 199] \mu\text{s}$, scaled to account for the difference in Δt range size. Imposing the constraint $\Delta t > 18 \mu\text{s}$ to preclude muon-Michel electron pairs from affecting the cuts, the signal-to-noise ratio S_0 is maximized for $\mathcal{E}_{\text{ref}} = [26, 60] \times 10^3$ adc and $\mathcal{T}_{\text{ref}} = [18, 48.1] \mu\text{s}$. Using the rough energy scaling discussed above, the \mathcal{E}_{ref} range falls around $[2.6, 6]$ MeVee, which overlaps with the Gd gamma-shower range after folding in the detector response.

With the Δt cut set to \mathcal{T}_{ref} , the cut on E_2 is derived for each two-week interval so that the same muon-induced neutron rate as in the reference period is maintained. To do this, we first create the background-subtracted Δt -vs.- E_2 histogram $H_S(E_2, \Delta t)$. The mean uncorrelated background $B(E_2)$ per Δt bin as a function of the E_2 bins is computed from the $\Delta t = [100, 199] \mu\text{s}$ range of the total histogram $H_T(E_2, \Delta t)$ of Fig. 8. Thus, $H_S(E_2, \Delta t)$ is obtained by subtracting $B(E_2)$ from each $(E_2, \Delta t)$ bin of $H_T(E_2, \Delta t)$. Fig. 11 shows the Δt -projections of $H_S(E_2, \Delta t)$ for $E_2 \in \mathcal{E}_{\text{ref}}$ corresponding to the reference beam-off data and to two weeks of beam-on data. The beam-on data Δt -projection clearly shows more counts in the integration range \mathcal{T}_{ref} . Next, we derive the adjusted cut $\mathcal{E}_{\text{adj}} \equiv [E_2^{\text{min}}, E_2^{\text{max}}]$ by minimizing the χ^2 between the reference and the two-week Δt -projection histograms, summing over the $\Delta t \in \mathcal{T}_{\text{ref}}$, while keeping a fixed E_2 range width $E_2^{\text{max}} - E_2^{\text{min}} = (60 - 26) \times 10^3$ adc. For the two-week beam-on data of Fig. 11, adjusting the E_2 range to $[29, 63] \times 10^3$ adc matches the muon-induced neutron rate to the reference value.

The two-week net counts after applying the \mathcal{E}_{adj} cuts computed for each two-week data interval are shown in Fig. 10. The result demonstrates that the calculated \mathcal{E}_{adj} cuts appropriately offset the spectrum shifting effect due to the HOG background pile-up and therefore can be used to compute the beam-induced neutron rates. Moreover, these \mathcal{E}_{adj} cuts also correct for the gradual gain drift that appears to have occurred over the several months of 2018 MARS operation; they would also correct for other possible PMT-response changes that may have occurred during the beam-on periods but that would be masked by the variability of the HOG-background shifting effect on the spectrum. The E_2^{min} computed for each two-week interval, also shown in Fig. 10, is distributed with a relative standard deviation $\sigma_{E_2^{\text{min}}}/\mu_{E_2^{\text{min}}} = 6\%$, which represents an estimate of the additional energy smearing due to gain variations and variability in the HOG-background-induced spectral shifts when all the 2018 beam-on data is considered. An advantage of this approach is that, as long as the detector data have been collected under the same overburden and incident cosmic-ray rate of the reference period, the same muon-induced neutron reference rate can be used to determine the E_2 cuts in adc units, since such adjusted ranges will correspond to equivalent physical energy ranges in MeVee units.

5 Measured BRN rate

Any SNS-target neutrons produced during beam POT events and that reach MARS would interact within a $2\ \mu\text{s}$ “beam” time window T_{beam} , preceded by an event-61 signal. The event-39 timestamp is offset by $800\ \mu\text{s}$ in the acquisition software so that the beam-neutron candidate pairs are constrained by $t_1 \in T_{\text{beam}} = [800.0, 802.0]\ \mu\text{s}$. The beam-on data t_1 histograms of Fig. 12 clearly shows the beam neutron spike at T_{beam} for pairs with Δt and E_2 within cuts consistent with Gd neutron capture. In order to estimate the steady-state background events in T_{beam} , we compute the number of pairs in a long out-of-beam strobe window $t_1 \in T_{\text{strobe}} = [1, 15]\ \text{ms}$, which is justified by the flat count profile within that window. A third $2\ \mu\text{s}$ out-of-beam window $T_{\text{check}} = [1000.0, 1002.0]\ \mu\text{s}$ illustrates that steady-state background statistical fluctuations are consistent with the mean background from the T_{strobe} and do not explain the T_{beam} neutron pair excess obtained below.

Fig. 13 shows the two-week interval counts for t_1 restricted to time windows T_{beam} , T_{strobe} and T_{check} respectively, E_2 obeying the two-week \mathcal{E}_{adj} cuts derived in section 4.1, and Δt within the Gd neutron-capture cut $\mathcal{T} = [6, 48.1]\ \mu\text{s}$. The Δt cut was extended down to $6\ \mu\text{s}$, which is about the time fast neutrons take to thermalize in MARS and their Gd capture probability to reach its highest value [16, 28]. To estimate the steady-state background contribution during the beam window, the T_{strobe} counts have been scaled by $T_{\text{beam}}/T_{\text{strobe}}$. For both beam operating periods (May 14-August 5 and August 23-November 17), the total counts in T_{beam} are consistently larger than the average background counts estimated from T_{strobe} . The counts in T_{check} are, on the other hand, consistent with background fluctuations.

The residual between the T_{beam} counts and the scaled T_{strobe} counts, representing our estimate of the beam neutron counts in MARS, is presented in the top panel of Fig. 14. Since the beam neutron rate is expected to be correlated with beam power, the counts in the middle panel of Fig. 14 have been normalized by the integrated beam power delivered during each corresponding two-week data-integration interval; if the delivered energy is zero, the beam-energy-normalized counts are

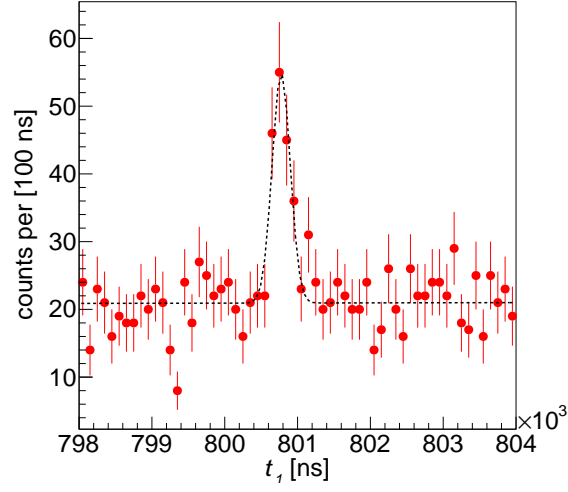


Figure 12. Histogram of the time interval t_1 between the first pulse of the pair, or prompt pulse, and an SNS-provided 60-Hz signal, named event-39. The histogram entries correspond to event pairs from the May-December 2018 data satisfying the neutron-capture cuts for Δt and E_2 ($\Delta t \in \mathcal{T}$ and E_2 obeying the two-week \mathcal{E}_{adj} cuts), and with a preceding SNS-provided signal, named event-61, supplied during beam-on operation whenever there is a POT event. The x-axis has been zoomed around the time window $T_{\text{beam}} = [800.0, 802.0] \mu s$ that contains the beam-neutron candidate pairs. The Gaussian fit results in a full width at half maximum $\text{FWHM} = 298 \pm 50$ ns, consistent with the SNS beam time profile.

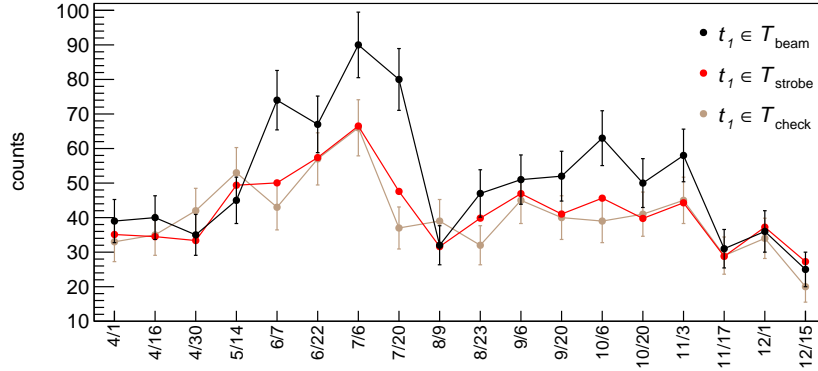


Figure 13. The two-week interval counts for event pairs with $\Delta t \in \mathcal{T}$, satisfying the two-week \mathcal{E}_{adj} cuts and t_1 restricted to time windows T_{beam} , T_{strobe} and T_{check} . The T_{strobe} counts have been scaled by $T_{\text{beam}}/T_{\text{strobe}}$. Error bars are statistical.

set to zero. The bottom panel of Fig. 14 presents the counts normalized instead by the duration of each data-integration interval.

Fig. 15 presents the Δt and E_2 histograms for all the 2018 data, after respectively applying the neutron-capture \mathcal{E}_{adj} and \mathcal{T} cuts, and for the three t_1 windows under consideration. The “ T_{beam} ” histograms consistently show event excesses within the respective neutron-capture regions, compared to the background histograms for the T_{strobe} and T_{check} windows. The Δt residual excess, shown in the bottom panel of Fig. 15, seems to extend only up to $\sim 30 \mu\text{s}$, which is shorter than the \mathcal{T} cut, indicating that this cut can be further tuned to potentially enhance the signal-to-background ratio. The E_2 residual excess, on the other hand, seems to end somewhere around 6×10^4 adc, closely matching the adjusted \mathcal{E} ranges.

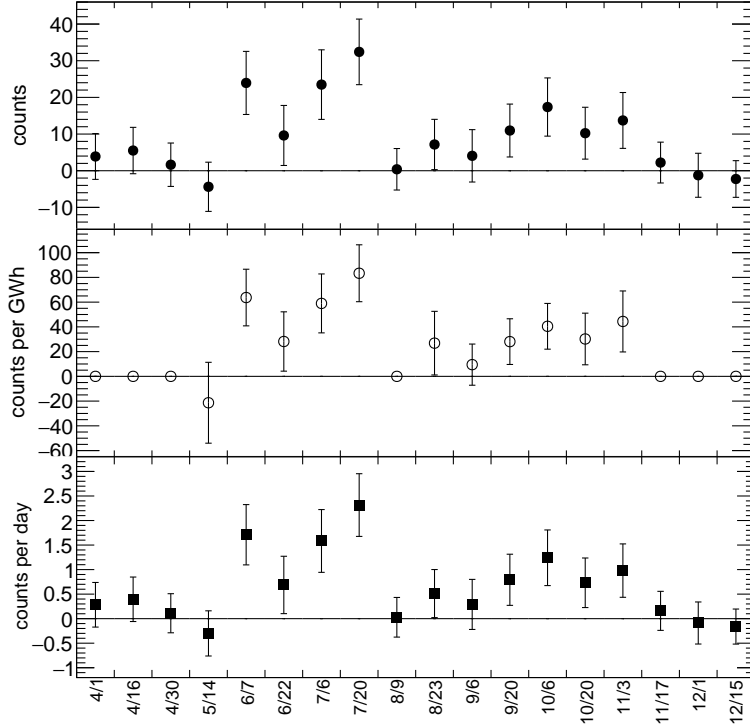


Figure 14. Top: the two-week-interval residual between the T_{beam} counts and the scaled T_{strobe} counts. Middle: residual counts normalized by the integrated beam power delivered during each corresponding two-week data-integration interval. Bottom: residual counts normalized by the exact duration of each data integration interval. Error bars are statistical.

Lastly, the left panel of Fig. 16 shows the deposited prompt energy E_1 for all the 2018 data satisfying the Gd neutron capture cuts. The E_1 residual excess during T_{beam} , presented in the right panel of Fig. 16, is highly suppressed beyond $\sim 8 \times 10^4$ adc, which approximately corresponds to 8 MeVee, or ~ 15 MeV in proton recoil energy. As noted in section 4.1, the gain variations and the HOG-background-induced spectral shift variability encountered in the 2018 beam-on data should contribute an additional $\sim 6\%$ to the energy smearing of the E_2 and E_1 histograms of Fig. 15 and 16.

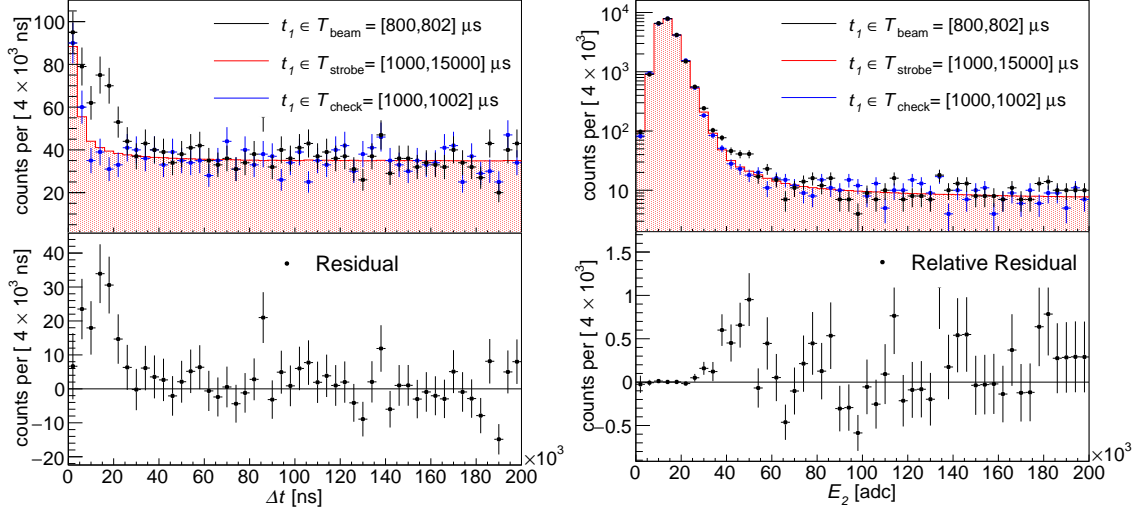


Figure 15. Top left: the Δt histogram for event pairs satisfying the two-week \mathcal{E}_{adj} cuts and with a preceding event-61 signal. Top right: the E_2 histogram for event pairs with $\Delta t \in \mathcal{T}$ and with a preceding event-61 signal. Bottom left: residual between the T_{beam} and the T_{strobe} Δt -histograms. Bottom right: residual between the T_{beam} and the T_{strobe} E_2 -histograms, divided by the T_{beam} histogram bin content. All the May-December 2018 data is included.

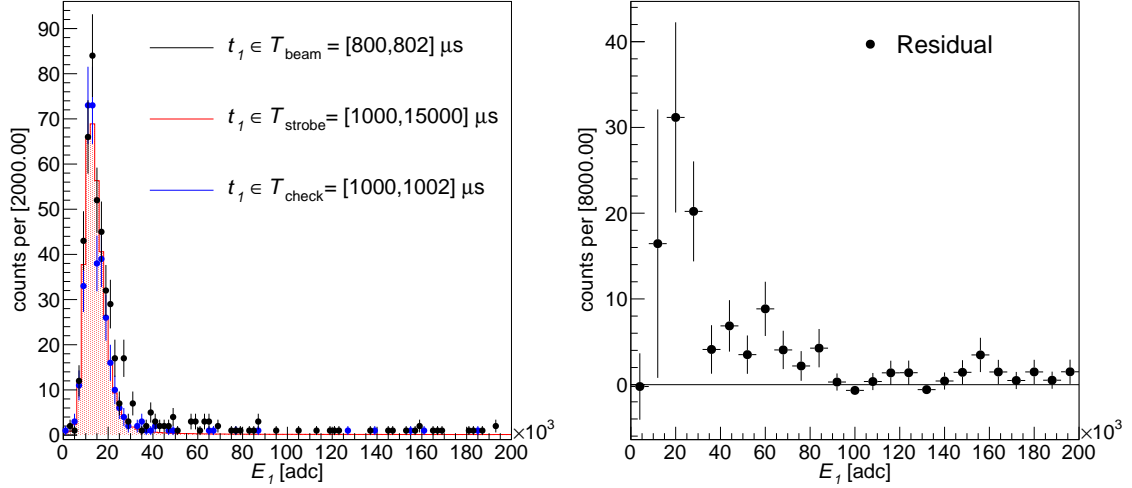


Figure 16. Left: The E_1 histogram for event pairs with $\Delta t \in \mathcal{T}$, satisfying the two-week \mathcal{E}_{adj} cuts, and with a preceding event-61 signal, from May-December 2018 data. Right: residual between the T_{beam} and the T_{strobe} histograms.

6 BRN flux at the Neutrino Alley

A total of 148.6 ± 26.0 neutron counts were detected within the $2 \mu s$ beam window in 154 beam-on days when the total POT delivered energy was 3.872 gigawatt-hour (GWh). To estimate the BRN flux incident on MARS from these data, we use the neutron detection efficiency measured with a deuterium-tritium (DT) neutron generator. Next, we describe this measurement and derive the detection efficiency for 14 MeV neutrons, albeit with a large uncertainty. A careful analysis of the DT generator data combined with the detector-response modeling will be treated in a separate publication.

6.1 Flux estimation from MARS data

The MARS detector was irradiated with a Thermo API120 neutron generator [29], on October 24th 2019 during a beam-off week. The generator employs the associated particle imaging (API) technique [30, 31], where the 3.5 MeV alpha particle produced by the D-T reaction in time coincidence and angular correlation with a 14 MeV neutron is detected by a 100 micron thick YAP:Ce crystal mounted on a fiber-optic faceplate. The scintillation light is collected by a Hamamatsu H13700 multi-anode flat panel PMT coupled to a resistor network producing four scaled outputs enabling reconstructing of the position via Anger-logic [32]. The direction of the associated neutron is determined within any one of 32×16 angular pixels, each subtending a 4.5 degree opening-angle cone.

The neutron-generator target was placed 117 cm perpendicular from the MARS side face, at three different vertical and horizontal offsets from MARS' center. Here, we only employ the data collected when the target was aligned with MARS' center such that the solid-angle region spanned by the alpha-tagged 14 MeV neutrons was within the horizontal edges of the MARS scintillator volume but slightly extended beyond the vertical edges. This is illustrated in Fig 17 (left) which shows the projection of the alpha-sensor pixel centers onto MARS' front plane as well as the projection of the neutron cone for only the central pixel. Only alpha triggers for which the collected energy is within $\pm 20\%$ of the full 3.5 MeV energy are included, which rejects incorrect triggers due to target-emitted x-rays.

The generator was run at its lowest power setting yielding $\sim 10^6$ n/s. Due to the higher event rate (25 kHz) compared to regular operation, the inter-pulse window to form MARS pairs was reduced to $\Delta t < 100 \mu s$. The prompt pulses generated by alpha-coincident 14 MeV neutrons create a sharp spike at $t_1 \in T_{DT} = [430, 490]$ ns, where t_1 is here defined as the time from the first pulse of the pair to the preceding alpha trigger. The E_1 energy distribution of fully thermalized 14 MeV neutrons peaks at around 4 MeVee, above the ~ 1 MeVee MARS threshold and is thus not affected by the gain decrease observed in these data. The adjusted range $\mathcal{E}_{DT} = [23, 57] \times 10^3$ adc is determined by matching the same reference muon-induced neutron rate of section 4.1 with the muon-induced neutron rate of the beam-off week immediately before this measurement. The rate of uncorrelated background pairs within the signal range $\Delta t \in \mathcal{T}$ is determined from the uncorrelated-background range $\Delta t \in [80, 95] \mu s$, in a similar fashion as in section 4.1.

The neutron-detection efficiency is defined as the ratio of the number of detected and incident neutrons. The number of incident neutrons is estimated as the count of alpha triggers that pass the alpha energy cut. The number of detected neutrons is the count of background-subtracted pairs

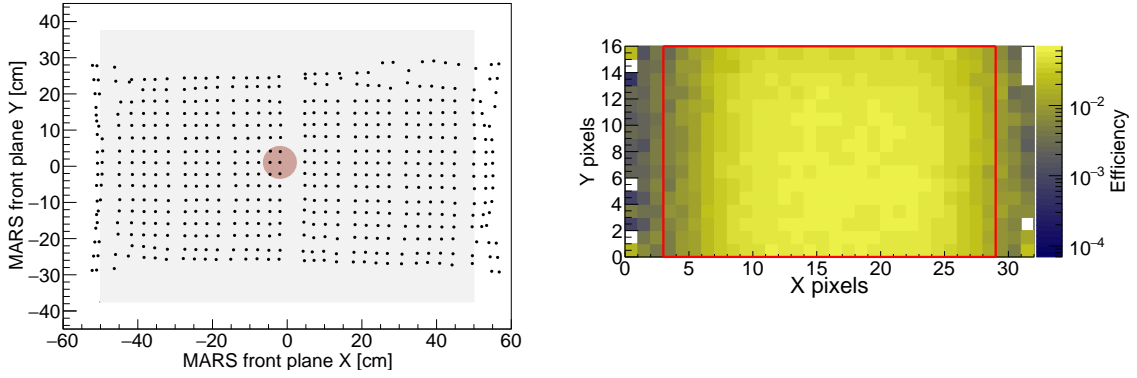


Figure 17. Left: Black dots are the projection of the alpha-sensor pixel centers onto MARS’ front plane in gray; the red circle is the projection of the 4.5 degree opening-angle neutron cone corresponding to the central pixel. Right: Efficiency computed for each alpha sensor pixel; the red rectangle delineates the pixels used to estimate the overall efficiency.

following the selected alpha triggers, and with $t_1 \in T_{DT}$, $\Delta t \in \mathcal{T}$ and $E_2 \in \mathcal{E}_{DT}$. The right panel of Fig. 17 shows the efficiency computed for each alpha sensor pixel, where the red rectangle delineates the pixels whose projections fall on the MARS face. The inside pixels next to MARS’ vertical edges have highly suppressed efficiency values due to a higher chance for the incident neutrons to escape the detector before being captured and for the Gd gammas to escape if the neutron is captured, but also due to the incomplete overlap of the neutron cones corresponding to the near-edge pixels. A careful treatment of these data, to be presented in future work, will determine the partial overlap of the edge neutron cones and will accordingly correct the number of incident neutrons.

In order to provide an estimate of MARS detection efficiency, we simply average the efficiency of all inside pixels. The systematic uncertainty due to the efficiency non-uniformity is estimated as the standard deviation of the inside pixels’ efficiency values, and represents the dominant contribution to the overall uncertainty. Contributions from the t_1 and E_2 cuts are smaller by two orders of magnitude. This results in an efficiency to detect 14 MeV neutrons equal to $(4.22 \pm 1.82)\%$. Furthermore, to obtain an estimate of the incident BRN flux from the measured rate, we employ this efficiency value as an approximation of the average capture-gated detection efficiency. We estimate 1.20 ± 0.56 BRN/m²/MWh incident on MARS at the center of the Neutrino Alley.

The proper approach to unfold the incident BRN flux is to model and validate MARS response as a function of energy. Using a preliminary Geant4 model of the MARS capture-gated signature that closely matches the 14 MeV neutron detection efficiency at the center of the detector, and assuming that the incident BRN flux follows a power-law energy dependence with exponent $\alpha = -1.5$ taken from the BRN flux study in [33], we calculate that the 14 MeV detection efficiency could be overestimating the flux-weighted average efficiency by about 50%. Our reported 14 MeV efficiency value already contains an error of that magnitude, mainly due to the inaccurate treatment of the near-edge pixel data. Future detector modeling and experimental validation work should reduce the BRN flux uncertainty due to the detection efficiency and will be the subject of a separate publication.

Table 1. BRN fluxes measured by several neutron detectors in the SNS basement corridor. These measurements indicate that the BRN flux in the center of the Neutrino Alley is largely suppressed compared to the BRN flux reaching the alcove.

Detector	Neutrino Alley location, see Fig. 3	BRN flux $\text{n/m}^2/\text{MWh}$	Uncertainty %
MARS	center	1.2	47
NSC	center left	5	> 50
NSC	alcove wedge	3×10^2	> 50
SciBath	alcove wall	1.3×10	19

6.2 Flux estimation from other detectors

Table 1 summarizes the BRN fluxes measured by several neutron detectors along the SNS basement corridor per megawatt-hour (MWh) of beam energy. A 2015-2016 measurement of the beam neutrons at a neighboring neutrino alley location with a scintillator-based neutron double-scatter camera (NSC), depicted in Fig. 3, produced a flux estimate of 5.3 beam neutrons/ m^2/MWh above 5 MeV within a $1.3 \mu\text{s}$ beam window [14]. The uncertainty on the NSC flux value is estimated to be larger than 50%, due to the NSC data’s poor statistics (only four double-scatter counts were recorded in about five beam-on months) and the significant uncertainty on the instrument’s poor double-scatter detection efficiency. A 2014 NSC measurement in the alcove at the end of the Neutrino Alley, also represented in Fig. 3, produced 272.1 beam neutrons/ m^2/MWh , *i.e.*, an almost two orders of magnitude larger flux. The 2015 data collected with the SciBath detector [34], also at the Neutrino Alley alcove, resulted in 13.3 beam neutrons/ m^2/MWh above 5 MeV within the $1 \mu\text{s}$ beam window used in that analysis. Despite the variation among the flux estimations by the different detectors, they consistently indicate a much larger BRN flux at the alcove compared to a quieter BRN flux at the Neutrino Alley center. MARS operation in the alcove area, which is already in progress, will be essential in quantizing the differences in the BRN intensity and spectrum between the alcove and the Neutrino Alley center.

7 Conclusions

We have described the analysis and results of the first dataset collected with the MARS detector at the SNS. We showed that the intense 511 keV gamma-ray background present during beam-on periods has the effect of not only increasing the overall event rate but also shifting the MARS energy spectrum to the right of the energy axes. We presented a method to offset the variable spectral shifts by adjusting the energy cuts so that the rate of muon-induced neutron events is kept at the same reference value for any data with the same cosmic overburden, where the reference rate is computed from five beam-off weeks from April 1 to May 6, 2018.

Our results show that the MARS detector is able to monitor the low BRN flux at the center of the Neutrino Alley under nominal SNS operations. The measured prompt spectrum decreases with deposited energy up to 8 MeVee, which corresponds to ~ 15 MeV of incoming neutron energy. To properly unfold the BRN spectral flux, the detection-efficiency energy dependence must be used. In that regard, the modeling and experimental validation of MARS response as a function of incoming

neutron energy will be the subject of a separate publication. However, our preliminary simulations show that the fraction of purely elastic capture-gated neutron events substantially declines with neutron energy, indicating that this detection mode will not provide meaningful bounds on the BRN spectra above a few tens of MeV. The full 22-week exposure of this dataset yields a 17% statistical uncertainty on the total BRN count, while a 2-week integration results in a mean of 14 BRN counts per 2-week interval with 58% statistical uncertainty. Sensitivity to the 7% difference in the operational beam power between the two 2018 beam periods (1.3 MW from May to June and 1.4 MW from September to November) would have required about 2.6 years of exposure under the signal and background levels in the Neutrino Alley center location.

While the results among different detectors presented in table 1 vary broadly, they revealed that the BRN flux at the center of the SNS basement corridor is suppressed by at least one order of magnitude compared to the alcove's BRN flux. To understand the origin of this excess, we are examining the possible paths for neutrons from the SNS target to Neutrino Alley, and are assessing the amount and location of bulk materials attenuating this flux. Further dedicated BRN measurements in the basement alcove are underway, including operating MARS in this location. Under a BRN flux at least one order of magnitude larger—and assuming a background rate as in the basement corridor center—less than a week of MARS data collection in the alcove would suffice to achieve the same 17% statistical uncertainty on a BRN count measurement.

Acknowledgments

The COHERENT collaboration acknowledges the resources generously provided by the Spallation Neutron Source, a DOE Office of Science User Facility operated by the Oak Ridge National Laboratory. This work was supported by the US Department of Energy (DOE), Office of Science, Office of High Energy Physics and Office of Nuclear Physics; the National Science Foundation; the Consortium for Nonproliferation Enabling Capabilities; the Institute for Basic Science (Korea, grant no. IBS-R017-G1-2019-a00); the Ministry of Science and Higher Education of the Russian Federation (Project “Fundamental properties of elementary particles and cosmology” No. 0723-2020-0041); the Russian Foundation for Basic Research (Project 20-02-00670_a); and the US DOE Office of Science Graduate Student Research (SCGSR) program, administered for DOE by the Oak Ridge Institute for Science and Education which is in turn managed by Oak Ridge Associated Universities. Sandia National Laboratories is a multi-mission laboratory managed and operated by National Technology and Engineering Solutions of Sandia LLC, a wholly owned subsidiary of Honeywell International Inc., for the U.S. Department of Energy's National Nuclear Security Administration under contract DE-NA0003525. The Triangle Universities Nuclear Laboratory is supported by the U.S. Department of Energy under grant DE-FG02-97ER41033. Laboratory Directed Research and Development funds from Oak Ridge National Laboratory also supported this project. This research used the Oak Ridge Leadership Computing Facility, which is a DOE Office of Science User Facility.

We acknowledge the NMDB database (www.nmdb.eu), founded under the European Union's FP7 programme (contract no. 213007) for providing data. The neutron monitor data from Newark/Swarthmore are provided by the University of Delaware Department of Physics and Astronomy and the Bartol Research Institute.

References

- [1] COHERENT collaboration, D. Akimov, J. B. Albert, P. An, C. Awe, P. S. Barbeau, B. Becker et al., *Observation of Coherent Elastic Neutrino-Nucleus Scattering*, *Science* **357** (2017) 1123–1126, [[1708.01294](#)].
- [2] COHERENT collaboration, D. Akimov et al., *COHERENT Collaboration data release from the first observation of coherent elastic neutrino-nucleus scattering*, [1804.09459](#).
- [3] COHERENT collaboration, D. Akimov, J. B. Albert, P. An, C. Awe, P. S. Barbeau, B. Becker et al., *COHERENT 2018 at the Spallation Neutron Source*, [1803.09183](#).
- [4] COHERENT collaboration, D. Akimov et al., *First Constraint on Coherent Elastic Neutrino-Nucleus Scattering in Argon*, *Phys. Rev. D* **100** (2019) 115020, [[1909.05913](#)].
- [5] COHERENT collaboration, D. Akimov et al., *First Measurement of Coherent Elastic Neutrino-Nucleus Scattering on Argon*, *Phys. Rev. Lett.* **126** (2021) 012002, [[2003.10630](#)].
- [6] COHERENT collaboration, D. Akimov et al., *COHERENT Collaboration data release from the first detection of coherent elastic neutrino-nucleus scattering on argon*, [2006.12659](#).
- [7] COHERENT collaboration, D. Akimov et al., *A D₂O detector for flux normalization of a pion decay-at-rest neutrino source*, [2104.09605](#).
- [8] COHERENT collaboration, D. Akimov et al., *Sensitivity of the COHERENT Experiment to Accelerator-Produced Dark Matter*, *Phys. Rev. D* **102** (2020) 052007, [[1911.06422](#)].
- [9] COHERENT collaboration, D. Akimov, P. An, C. Awe, P. S. Barbeau, P. Barton, B. Becker et al., *The COHERENT Experiment at the Spallation Neutron Source*, [1509.08702](#).
- [10] C. Roecker, A. Bernstein, N. Bowden, B. Cabrera-Palmer, S. Dazeley, M. Gerling et al., *Design of a transportable high efficiency fast neutron spectrometer*, *Nuclear Instruments and Methods in Physics Research Section A: Accelerators, Spectrometers, Detectors and Associated Equipment* **826** (2016) 21 – 30.
- [11] GEANT4 collaboration, S. Agostinelli et al., *GEANT4: A simulation toolkit*, *NIM A* **506** (2003) 250–303.
- [12] “SIS3316 16 channel VME digitizer family.” [Online] <http://www.struck.de/sis3316.html>.
- [13] “A toolkit for data acquisition control and analysis for waveform digitizers including GAGE, XIA, and Struck.” [Online] <https://code.ornl.gov/CASA/ngmdaq>.
- [14] B. Cabrera-Palmer, E. Brubaker, M. Gerling and D. Reyna, *Extension of the neutron scatter camera sensitivity to the 10-200 MeV neutron energy range*, *Review of Scientific Instruments* **90** (2019) 053305, [<https://doi.org/10.1063/1.5091715>].
- [15] S. Brice et al., *A method for measuring coherent elastic neutrino-nucleus scattering at a far off-axis high-energy neutrino beam target*, *Phys. Rev. D* **89** (2014) 072004, [[1311.5958](#)].
- [16] C. D. Roecker, *Measurement of the High-Energy Neutron Flux Above and Below Ground*. PhD thesis, U.C. Berkeley, 2016.
- [17] Grafana Labs, “Grafana Documentation.” [Online] <https://grafana.com/docs/>, 2018.
- [18] Z. Jian-Fu, R. Xi-Chao, H. Long, L. Xia, B. Jie, Z. Guo-Guang et al., *Measurements of the light output functions of plastic scintillator using $^9\text{Be}(d, n)^{10}\text{B}$ reaction neutron source*, *Chinese Physics C* **34** (jul, 2010) 988–992.

- [19] T. Laplace et al., *Low Energy Light Yield of Fast Plastic Scintillators*, *Nucl. Instrum. Meth. A* **954** (2020) 161444, [[2009.07217](#)].
- [20] PARTICLE DATA GROUP collaboration, K. A. Olive et al., *Review of Particle Physics*, *Chin. Phys.* **C38** (2014) 090001.
- [21] MICROBooNE collaboration, R. Acciarri et al., *Michel Electron Reconstruction Using Cosmic-Ray Data from the MicroBooNE LArTPC*, *JINST* **12** (2017) P09014, [[1704.02927](#)].
- [22] R. Hertenberger, M. Chen and B. L. Dougherty, *Muon induced neutron and pion production in an organic liquid scintillator at a shallow depth*, *Phys. Rev. C* **52** (1995) 3449–3459.
- [23] F. Boehm et al., *Neutron production by cosmic ray muons at shallow depth*, *Phys. Rev. D* **62** (2000) 092005, [[hep-ex/0006014](#)].
- [24] Y.-F. Wang, V. Balic, G. Gratta, A. Fassò, S. Roesler and A. Ferrari, *Predicting neutron production from cosmic-ray muons*, *Phys. Rev. D* **64** (Jun, 2001) 013012.
- [25] L. Garrison, *Measurement of Neutron and Muon Fluxes 100 m Underground with the SciBath Detector*. PhD thesis, Jan, 2014. 10.2172/1151758.
- [26] J. M. Clem and L. I. Dorman, *Neutron monitor response functions*, *Space Science Reviews* **93** (2000) 335–359.
- [27] “Newark/Swarthmore Neutron Monitor.” [Online] <https://www.nmdb.eu/>.
- [28] N. Bowden, M. Sweany and S. Dazeley, *A note on neutron capture correlation signals, backgrounds, and efficiencies*, *Nuclear Instruments and Methods in Physics Research Section A: Accelerators, Spectrometers, Detectors and Associated Equipment* **693** (2012) 209 – 214.
- [29] “Thermo Fisher Scientific API 120 Neutron Generator.” [Online] <https://www.thermofisher.com/>.
- [30] D. Chichester, M. Lemchak and J. Simpson, *The api 120: A portable neutron generator for the associated particle technique*, *Nuclear Instruments and Methods in Physics Research Section B: Beam Interactions with Materials and Atoms* **241** (2005) 753–758.
- [31] A. Beyerle, J. P. Hurley and L. Tunnell, *Design of an associated particle imaging system*, *Nuclear Inst.and Methods in Physics Research, A* **299** (1990) 458–462.
- [32] H. O. Anger, *Scintillation camera with multichannel collimators*, *Journal of Nuclear Medicine (U.S.)* **5** (7, 1964) .
- [33] G. C. Rich, *Measurement of Low-Energy Nuclear-Recoil Quenching Factors in CsI[Na] and Statistical Analysis of the First Observation of Coherent, Elastic Neutrino-Nucleus Scattering*. PhD thesis, The University of North Carolina at Chapel Hill, Jan., 2017.
- [34] M. R. Heath, *A First Search for Coherent Elastic Neutrino-Nucleus Scattering with Liquid Argon*. PhD thesis, Indiana U., Bloomington (main), 2019. 10.5967/jmrj-9078.